Negative spin polarization of Mn_2VGa Heusler alloy thin films studied in current-perpendicular-to-plane giant magnetoresistance devices

Hirofumi Suto*, Vineet Barwal, Kodchakorn Simalaotao, Zehao Li, Keisuke Masuda, Taisuke Sasaki, Yoshio Miura, and Yuya Sakuraba

[1]Research Center for Magnetic and Spintronic Materials, National Institute for Materials Science (NIMS), Tsukuba, 305-0047, Japan

SUTO.Hirofumi@nims.go.jp

ABSTRACT

Magnetic materials with high negative spin polarization have been sought as a building block to increase the design freedom and performance of spintronics devices. In this paper, we investigate negative spin polarization of Mn_2VGa Heusler alloy in current-perpendicular-to-plane giant magnetoresistance (CPP-GMR) devices. We fabricated an epitaxial CPP-GMR stack consisting of Mn_2VGa/Ag/CoFe with $L2_1$ ordering in the Mn_2VGa layer and observed negative magnetoresistance (MR), which provided evidence of negative spin polarization. The MR ratio depended on thermal treatments (deposition at an elevated temperature and post-annealing), because these processes affected the ordering, roughness, and magnetic properties of Mn_2VGa. The maximum MR ratio reached −1.8% at room temperature and −3.0% at low temperature, representing the highest among the negative MR values in pseudo-spin-valve CPP-GMR devices despite the underestimation due to an incomplete antiparallel magnetization configuration. These findings demonstrate the potential of Mn_2VGa for a material with high negative spin polarization.

I. INTRODUCTION

Material research has played a crucial role in improving the performance of spintronic devices. One key research direction has been the search for materials with high spin polarization, because these materials can significantly enhance magnetoresistance (MR) and spin-transfer torque (STT) efficiency, which are the main operation principles of the spintronic devices [1–7]. For example, Co-based Heusler alloys, predicted to possess +100 % spin polarization, have been extensively studied and have experimentally demonstrated very high MR ratios [8–15]. On the other hand, another research direction into negative spin polarization materials has also gained recent attention. In negative spin polarization materials, the spin momentum direction of the spin-polarized conduction electron is opposite to the magnetization direction [16,17]. This relation is in contrast to the standard positive spin polarization found in the aforementioned Co-based Heusler alloys and many other spintronic materials. Intriguingly, negative spin polarization materials can reverse the signs of MR and STT. In particular, negative STT can realize new device structures by exerting STT of the desired spin direction and improve their performance beyond the limitation of conventional positive spin polarization materials. This characteristic is advantageous to devices demanding strong STT, such as spin-torque oscillators for energy-assisted writing in hard-disk-drive applications, in which oscillation of large magnetic volume is crucial [18–23].

Tunnel magnetoresistance (TMR) studies on Fe_4N and Fe_3O_4 have reported large negative MR over −50% at room temperature, demonstrating the negative spin polarization of these materials [24,25]. Similarly, giant magnetoresistance (GMR) studies reported that materials such as CoFeGd, FeCr, FeV, NiCr, and Fe_4N have negative spin polarization [16,26–29]. However, the amplitude of the reported negative MR ratio is smaller than −1% at room temperature in the case of pseudo-spin-valve current-perpendicular-to-plane (CPP)-GMR devices, indicating the small negative spin polarization of these materials. Considering that negative STT is beneficial to devices demanding strong STT, implementation of negative spin polarization in CPP-GMR devices is highly demanded for practical applications because their all-metallic structure can withstand higher current density than TMR devices.

Mn_2VGa (MVG) belongs to Mn-based Heusler alloys and is a promising candidate for a negative spin polarization material [30–36]. The calculated density of states has a pseudo gap in the majority-spin band, from which high negative spin polarization is expected [33–35]. In addition, its Curie temperature of ~784 K is sufficiently high for room temperature operation. The saturation magnetization (M_s) is small due to the ferrimagnetic configuration of the Mn and V moments, and this property is suitable for hard disk drive applications because the small stray fields from small M_s materials can minimize disturbance to the writing field [22,37]. Klewe, et al. [32] fabricated TMR devices using a sputter-deposited epitaxial stack consisting of MgO(001) substrate/MVG/MgO barrier/$Co_{0.7}Fe_{0.3}$ and confirmed negative MR, providing evidence of negative spin polarization in MVG. However, no study has been reported on CPP-GMR devices.

In this study, we investigated the negative spin polarization of MVG in epitaxial CPP-GMR devices. We fabricated GMR devices with MVG and CoFe magnetic layers with a Ag spacer and demonstrated a negative MR ratio of –1.8% at room temperature. A tungsten layer provides a suitable template that enables a high-quality epitaxial MVG layer to grow and stops the interdiffusion between the MVG layer and the low resistance Ag bottom electrode. Deposition of the MVG layer at an elevated temperature followed by post-annealing can enhance the ordering and negative spin polarization of MVG while maintaining the flatness of the GMR film. These results demonstrated the potential of MVG as a high-performance negative spin-polarization material.

II. EXPERIMENTAL AND COMPUTATIONAL METHODS

We prepared the following three series of samples by magnetron sputtering on MgO(001) substrates: (A) single-layer MVG films, (B) MVG films on bottom electrodes, and (C) CPP-GMR stacks with an MVG layer. The numbers in the parentheses in the following are thickness in nanometers. The series-A samples were composed of MVG (37)/Al (2), in which the MVG layers were deposited directly on MgO substrates and passivated by an Al layer. The series-B samples were composed of a bottom electrode/ MVG(37) / Al(2), where the bottom electrodes were Cr(5) / Ag(50), Cr(5) / Ag(50) / V(5), and Cr(5) / Ag(50) / Cr(5) / W(15). The series-C samples were composed of Cr(5) / Ag(80) / Cr(5) / W(15) / MVG(10) / Ag(7) / $Co_{50}Fe_{50}$(7) / Ag(5) / Ru(8). The MVG layers were deposited by co-sputtering from $Mn_{55}Ga_{45}$ and V targets at elevated substrate temperatures (T_s) ranging from 300°C to 600°C. In some samples, the MVG layers were additionally post-annealed at a temperature (T_p) of 500°C for 30 min after the deposition. The layers above the MVG layer were deposited at room temperature after cooling down. The typical composition of the MVG layer was $Mn_{54.29}V_{20.45}Ga_{25.26}$, as measured by X-ray fluorescence (XRF) analysis calibrated by the standard sample whose composition was analyzed by inductively coupled plasma mass spectrometry. The MVG composition was adjusted to be Mn-rich and V-poor because this off-stoichiometric composition can achieve higher ordering [36]. In addition, anti-site of V atoms occupying the Mn site is detrimental to negative spin polarization according to the calculation [32], and a Mn-rich and V-poor composition can suppress such anti-sites [36].

The crystal structure and atomic ordering of the prepared films were investigated using X-ray diffraction (XRD) with a Cu–$K\alpha$ radiation source. The degree of $B2$ and $L2_1$ order (S_{B2} and S_{L2_1}) were calculated as $S_{B2} = \sqrt{\frac{I_{002}^{\mathrm{exp}}/I_{004}^{\mathrm{exp}}}{I_{002}^{\mathrm{sim}}/I_{004}^{\mathrm{sim}}}}$ and $S_{L2_1} = \sqrt{\frac{I_{111}^{\mathrm{exp}}/I_{444}^{\mathrm{exp}}}{I_{111}^{\mathrm{sim}}/I_{444}^{\mathrm{sim}}}}$, where I_{hkl}^{exp} and I_{hkl}^{sim} represent the experimental and simulated hkl peak intensities, respectively. In the XRD simulation, the off-stoichiometric composition was taken into account in the simulation model, where the excess Mn atoms simply occupy the deficient V sites. The magnetic properties of MVG were evaluated by measuring the curves of magnetization (*M*) versus magnetic field (*H*) using a vibrating sample magnetometer at room temperature. The M_s was estimated from the *M*-*H* curves. The surface morphology was measured using atomic force microscopy with a scan area of 1 μm × 1 μm, and the average roughness (R_a) and the peak-to-valley height (*P*-*V*) were calculated. The cross-sectional microstructure of the samples was analyzed using high-angle annular dark-field scanning transmission electron microscopy (HAADF-STEM), nano-beam electron diffraction (NBED), and energy-dispersive X-ray spectroscopy (EDS).

Pseudo-spin-valve CPP-GMR devices were fabricated using the following procedure. The series-C samples were patterned into circular and elliptical pillars with dimensions of 80 nm × 80 nm and 140 nm × 70 nm by electron-beam lithography and Ar ion milling. The pillars were then covered with a thin Ta adhesion layer and a SiO_2 passivation layer. After the lift-off of the covering layers, a Au top electrode was fabricated. For each device size, 75 devices were fabricated on one substrate. Resistance versus magnetic field (*R*-*H*) measurements were conducted using the four-probe method. All the devices were measured by an auto-prober system with an *H* range of 2.5 kOe at room temperature. A few devices were additionally measured by a physical properties measurement system using a higher *H* range and lower temperatures. The in-plane magnetic field was applied along the longitudinal direction of the elliptical pillars. The MR ratio was defined as $MR = (R - R_{\max})/R_{\max}$, where $R_{\max}$ is the maximum *R* in the measured *H* range.

The first-principles calculations for ballistic transmittance based on the Landauer formular [38] were performed using the QUANTUM ESPRESSO code [39,40]**.** For the exchange-correlation energy, we adopted the ultrasoft pseudopotential method and the Generalized Gradient Approximation [41]. A set of 10 × 10 × 1 grid of k-points is used for the Brillouin zone integrations. The cutoff energy for the wave function and charge density is set to 40 (Ry) and 400

(Ry), respectively. Stacking models of MVG/Ag/MVG(001) were constructed using tetragonal supercells, with the in-plane lattice parameter of the supercell fixed at a = 4.067 Å. The MVG/Ag(001) interface featured two types of termination: Mn termination and VGa termination. The stacking models consist of 7 atomic layers of Ag spacer, with 17 and 15 atomic layers of MVG for Mn termination and VGa termination, respectively.

III. RESULTS AND DISCUSSION

We first studied the epitaxial growth of MVG and the effect of T_s on the ordering using the series-A samples. Figure 1(a) shows the out-of-plane XRD profiles of the samples for T_s = 300ºC –600ºC. All the results indicate (001)-oriented growth, and the appearance of 002 superlattice peaks indicates the presence of $B2$ ordering. Figure 1(b) shows the corresponding XRD profiles along the [111] direction at χ = 54.7°. The appearance of 111 superlattice peaks indicates the presence of $L2_1$ ordering. Figure 1(c) shows the T_s dependence of S_{B2} and S_{L2_1}. The S_{B2} value was 0.8 already at T_s = 300ºC, which further enhances to 0.9 at T_s = 600ºC. The S_{L2_1} value monotonically increases with T_s and reaches 0.8 at T_s = 600ºC. The first-principles calculations [32,36] reported that $L2_1$-ordered and $B2$-ordered MVG have negative spin polarization, which is higher for the $L2_1$-ordered structure. The XRD results indicated that the experimental samples had relatively high ordering, from which high negative spin polarization can be expected.

We also examined the MVG growth on bottom electrodes using the series-B samples as a preliminary step to fabricate CPP-GMR stacks. The structures of the bottom electrodes were Cr (5)/Ag (50), Cr (5)/Ag (50)/V(5), and Cr (5)/Ag (50)/Cr (5)/W (15). We first used Cr/Ag bottom electrodes to fabricate CPP-GMR stack because Cr/Ag is the standard bottom electrode employed in studies on Heusler alloy-based CPP-GMR devices [12]. However, we found that the interdiffusion occurred between MVG and Ag (the results are shown in the supplementary material). Thus, we searched for a suitable bottom electrode structure. The diffusion problem between Mn and Ag is consistent with the report that Co_2MnZ-type Heulser alloys showed lower thermal stability with a Ag spacer than Co_2FeZ-type Heulser alloys [10]. In addition, the phase diagram of Ag-Mn system shows a certain amount of Mn is miscible to Ag at the annealing temperatures. Figures 1(d) and 1(e) show the out-of-plane and [111]-direction XRD profiles of the series-B samples for T_s = 500ºC, respectively. The XRD peaks indicate the (001)-oriented epitaxial growth of both bottom electrode and MVG layer in all the samples, regardless of the various lattice misfits with respect to the MVG lattice constant reported for bulk study: MgO (+0.9%), Ag (–2.2%), V (+2.6%), and W (+7%). Similar to the series-A samples, 002 and 111 superlattice peaks were observed indicating the presence of $B2$ and $L2_1$ ordering. In the case of the Cr/Ag/Cr/W bottom electrode, the S_{B2} and S_{L2_1} values were calculated to be 0.99 and 0.82, respectively, which were higher than those of the series-A sample at T_s = 500ºC. In this calculation the XRD results of the sample only with the Cr/Ag/Cr/W bottom electrode shown as the dashed line in Figs 1(d) and 1(e) were subtracted as a background. The order parameter of the sample with Cr/Ag and Cr/Ag/V bottom electrodes were not analyzed because the MVA layer on these bottom electrodes were not properly fabricated as discussed below by considering M_s of the MVG layers.

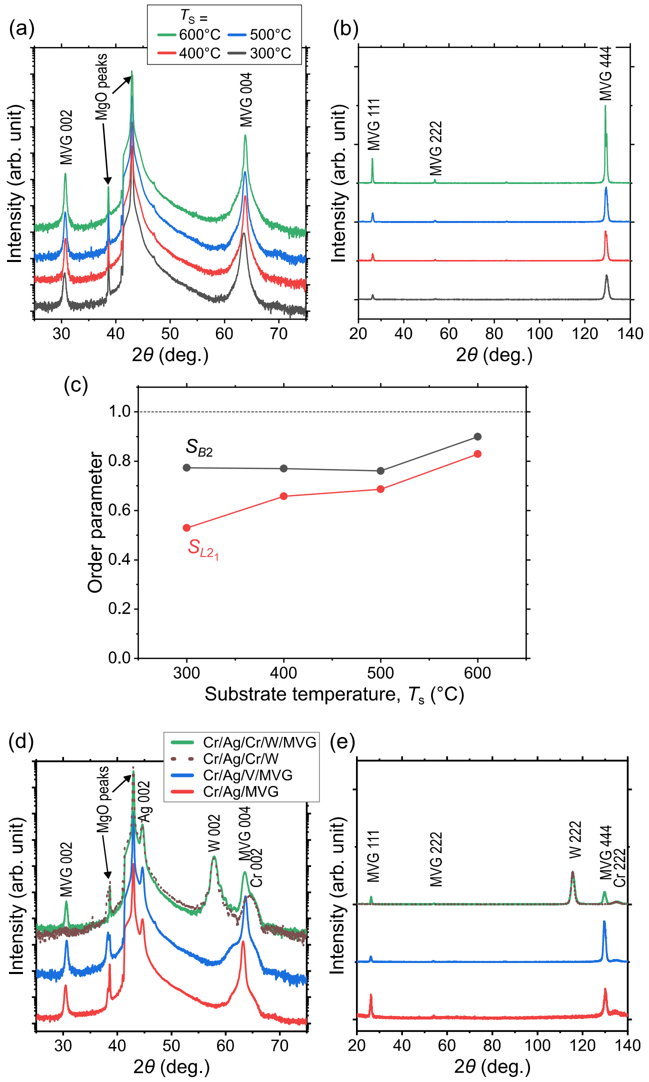

Fig. 1. (a) Out-of-plane and (b) [111]-direction XRD profiles for the series-A samples for T_s = 300ºC –600ºC. The legends are common for (a) and (b), and the data are offset for clarity. (c) The T_s dependence of S_{B2} and S_{L2_1} calculated from the peak intensities in (a) and (b). (d) Out-of-plane and (e) [111]-direction XRD profiles for the series-B samples with Cr/Ag, Cr/Ag/V, and Cr/Ag/Cr/W bottom electrodes for T_s = 500ºC. The data for the sample only with the Cr/Ag/Cr/W bottom electrode and without the MVG layer is also shown. The legends are common for (d) and (e), and the data are offset for clarity.

We next evaluated the magnetic properties of MVG. It has been reported that the saturation magnetization of MVG is sensitive to disorder because of the ferrimagnetic configuration of the Mn and V moments and thus can be a good indicator of the ordering [36]. Figure 2(a) shows the in-plane *M*-*H* curves of the series-A samples for T_s = 300ºC –600ºC. The *M*-*H* curves were similar for T_s = 300ºC and 400ºC with M_s of 120 emu/cc and a coercive field (H_c) of approximately 800 Oe. By further increasing T_s, the M_s increased to 190 emu/cc at T_s = 500ºC and 220 emu/cc at T_s = 600ºC, and the H_c decreased to 400 Oe at T_s = 600ºC. The M_s value is similar to those reported in the previous study of MVG thin films [36]. The M_s value estimated from the Slater-Pauling rule based on the XRF composition was approximately 300 emu/cc. The experimental values were smaller than the Slater-Pauling value reflecting the imperfect ordering. Although both M_s and order parameters showed an increasing trend with respect to T_s, the trend is not completely consistent. In the XRD results, S_{B2} and S_{L2_1} were almost the same between T_s = 400 and 500ºC, while M_s changed significantly between these temperatures. Although the reason for the inconsistency is unclear, this result suggests the importance of measuring both order parameters and M_s to evaluate the quality of the MVG films.

Figure 2(b) shows the T_s dependence of M_s of the series-A samples calculated from the results in Fig. 2(a). In addition, the M_s of the sample deposited at T_s = 300ºC and post-annealed at T_p = 500ºC is shown as an open square. The dashed line shows the M_s calculated from the Slater-Pauling rule. The M_s value for T_s = 300ºC + T_p = 500ºC was higher than those for T_s = 300 and 400ºC but lower than that for T_s = 500ºC, indicating that post-annealing at 500ºC improved the ordering, though it was not as effective as T_s of the same temperature. This additional post-annealing will be employed later in the series-C sample. Figure 2(b) also shows the results of the series-B samples. The M_s values for the three bottom electrode structures were measured at T_s = 500ºC. The M_s values of the Cr/Ag and Cr/Ag/V samples were significantly smaller than that of the series-A sample, indicating that these bottom electrode structures have a detrimental effect on the MVG growth. The reason for the small M_s of the Cr/Ag sample might be the interdiffusion between MVG and Ag, as discussed above. The reasons for the small M_s of the Cr/Ag/V sample might be interdiffusion between MVG and V, which disturbed the composition of MVG. In contrast, the M_s of the Cr/Ag/Cr/W sample was slightly higher than the series-A samples. The T_s dependence was measured for the Cr/Ag/Cr/W samples, which showed the similar trend to that of the series-A samples, indicating that the W layer provided a good template for the growth on MVG, despite the large misfit. Figure 2(c) shows the in-plane M-H curves of the Cr/Ag/Cr/W samples for T_s = 300ºC–600ºC. In comparison with the series-A samples, the H_c was high especially at lower T_s with H_c of ~2 kOe at T_s = 300 ºC. The saturation field (H_s) was also high being ~7 kOe at T_s = 300 ºC. We speculate that the large H_c and H_s might be due to the dislocations or lattice distortions at the interface between the MVG and W layers resulting from the large misfit, which functioned as pinning sites.

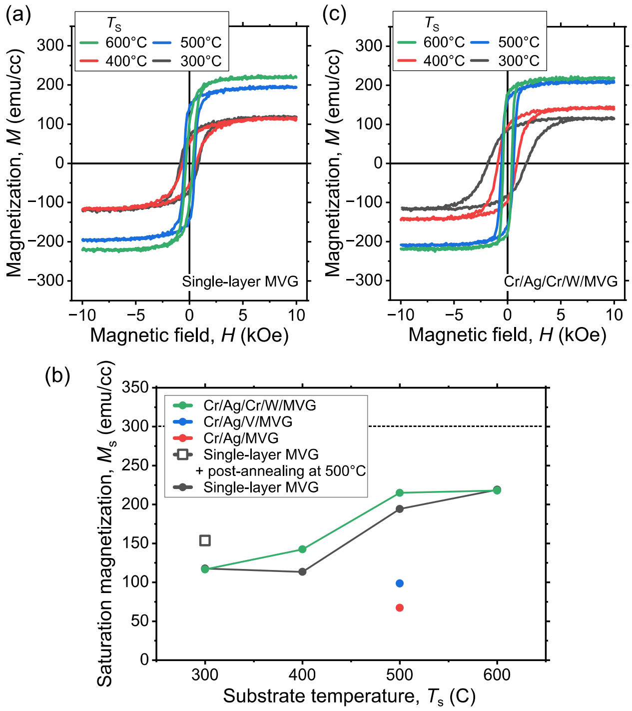

Fig. 2. (a) M-H curves of the series-A samples for T_s = 300ºC –600ºC. (b) Dependence of M_s on T_s for the series-A and series-B samples. The dashed line represents the value estimated from the Slater-Pauling rule. (c) M-H curves of the series-B samples with the Cr/Ag/Cr/W bottom electrode for T_s = 300–600ºC.

To demonstrate the negative spin polarization of MVG, we fabricated CPP-GMR stacks using the Cr/Ag/Cr/W bottom electrode. The structure is shown in Fig. 3(a). Figures 3(b) and 3(c) show the out-of-plane and [111]-direction XRD profiles of the series-C samples, respectively, for T_s = 300ºC–500ºC and T_s = 300ºC + T_p = 500ºC. 002 and 111 superlattice peaks were observed in all the samples. Figure 3(d) shows S_{B2} and S_{L2_1} calculated from the data in Figs. 3(b) and 3(c). The S_{B2} values indicate that the ordering was monotonically improved with increasing T_s and that additional post-annealing can improve the ordering. This result is consistent with that of the single-layer samples. The S_{L2_1} values show a similar trend except that the value was higher at T_s = 300ºC than T_s = 400ºC. A possible reason for this inconsistency is low accuracy because of the weak peak intensities at T_s = 300ºC. Here, we did not evaluate M_s of the samples because the thickness variations in the CoFe layer can cause large errors in the estimated M_s of the MVG layer because CoFe has much higher M_s than MVG. We also examined the surface morphology of the series-C samples. Figure 3(e) shows the R_a and P-V values with respect to the annealing conditions. For T_s = 300ºC and 400ºC, the films were sufficiently flat to fabricate the CPP-GMR devices. However, the flatness abruptly degraded at T_s = 500 ºC. The yield of the CPP-GMR devices from this film was low due to the roughness, which will be discussed later. On the other hand, the flatness for T_s = 300ºC + T_p = 500ºC was almost the same as that for T_s = 300ºC, indicating that the additional post-annealing did not degrade the flatness.

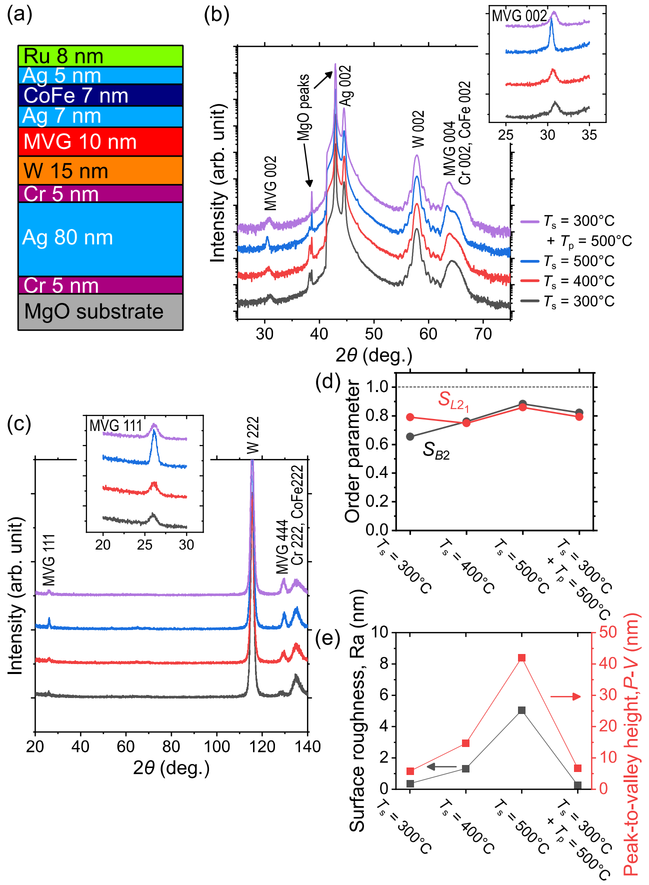

Fig. 3. (a) Structure of the series-C samples. (b) Out-of-plane and (c) [111]-direction XRD profiles of the series-C samples for T_s = 300ºC, 400ºC, 500ºC and T_s = 300ºC + T_p = 500ºC. The insets show the enlarged view around the MVG 002 and 111 peaks. The legends are common for (b) and (c), and the data are offset for clarity. (d) Annealing condition dependence of S_{B2} and S_{L2_1} calculated from the peak intensities in (b) and (c). (e) Annealing condition dependence of R_a and *P*-*V*.

We measured the *R*-*H* curves from the CPP-GMR devices fabricated from the series-C samples. Figures 4(a)–4(d) show examples of the *R*-*H* curves. The shapes of the *R*-*H* curves had large device-to-device variations within each sample, which can be attributed to the following reason. As shown in the *M*-*H* curves in Fig. 2(c), the magnetization of the MVG layer changed gradually with *H* with low squareness, indicating that the field response of the MVG magnetization was spatially non-uniform. Considering that the *R*-*H* curves reflected the local magnetic behavior of the small device area, we speculate that the distributions in the field response resulted in variations in the *R*-*H* curves. In addition, spatially non-uniform ordering of the MVG layer might lead to a distribution in the MR ratio because the spin polarization is affected by the ordering. The *R*-*H* curve in Fig. 4(a) for the upward *H* sweep can be interpreted as the schematics of the magnetization configurations shown above the figure. The abrupt *R* change around the zero field corresponds to the magnetization switching of the CoFe layer, and the slope of the *R* change switches from negative to positive at this point. This interpretation indicates negative MR in which *R* was higher (lower) when the magnetization configuration was more parallel (antiparallel). Note that plateau regions with lower *R* corresponding to a complete antiparallel configuration were not obtained, and the full MR ratio could not be evaluated. The negative MR provides evidence of negative spin polarization in the MVG layer because both bulk spin asymmetry of CoFe and interfacial spin scattering asymmetry of CoFe/Ag are positive [42]. The bulk and interfacial contributions to the negative spin polarization in the MVG layer cannot be separated in this experiment, and further study is necessary to understand these properties. In the previous TMR study on MVG reported similar *R*-*H* curves with an incomplete antiparallel magnetization configuration due to gradual change in the magnetization in the MVG layer [32].

The *R*-*H* curve in Fig. 4(a) exhibits hysteresis in the large *H* range and the downward and upward *H* sweeps coincide at around $H = \pm 18$kOe. Considering that the CoFe layer had small H_c, the shape of the *R*-*H* curve is determined by the magnetization behavior of the MVG layer, and the result indicated that the H_s of MVG layer was 18 kOe or higher, where the parallel configuration was obtained. This large H_s is, to some extent, consistent with the *M*-*H* curve of the series-B sample (Fig. 2(c)) in which the H_s was as high as 7 kOe at T_s = 300ºC. The difference in H_s between the *M*-*H* and *R*-*H* curves might be attributed to the different thickness of the MVG layer (37 nm in the series-B and 10 nm in the series-C sample). The large H_c and H_s were related to the interface with the W layer presumably due to the dislocations or lattice distortion originating from the large misfit between MVG and W. Thus, we speculate that the thinner MVG layer was more affected by the interface with the W layer, resulting in higher H_s. Additionally, patterning of the devices into nanopillars could affect the magnetization behavior due to pinning and different domain formation [43]. The inset shows the *R*-*H* curve in the *H* range used in the auto-prober measurements. Because the *R*-*H* was measured only in the minor loop, the curve was asymmetric, and the amplitude of MR ratio was smaller than that measured in the higher field range. Note that the statistical data of the MR ratio presented in the following paragraph were obtained from the minor loop. The *R* continued to change even at H = ±30 kOe, suggesting the existence of other small contributions to *R*.

In the *R*-*H* curve at T_s = 400ºC T_s = 500ºC and T_s = 300ºC + T_p = 500ºC shown in Figs. 4(b), 4(c), and 4(d), the downward and upward *H* sweeps coincide within the measurement field range, because higher T_s or post-annealing reduced the H_s of the MVG layer. In addition, the amplitude of the negative MR ratio increased. Figure 4(e) shows the summary of MR ratio obtained by auto-prober measurements of all the devices in each sample. The defective devices showing abnormal *R* were excluded. The distributions in *R* and MR ratio are presented in the supplementary material. The number of data points was significantly small in the case of T_s = 500ºC because of the low device yield, which might be due to the increased roughness. The MR ratio shows large distributions within each sample because of the shape variations in the *R*-*H* curves. When we excluded the T_s = 500ºC sample because of the lack of statistical data, the MR ratio increased in the following order: T_s = 300ºC, T_s = 400ºC, and T_s = 300ºC + T_p = 500ºC with the maximum negative MR ratio being ~−1.8 %. The resistance area product (RA) of the T_s = 300ºC + T_p = 500ºC sample was calculated to be 22 m$\Omega\cdot\mu$m^2. Figure 4(f) shows the measurement temperature dependence of the MR ratio for the $T_s = 300$ºC + $T_p = 500$ºC sample. The negative MR ratio was enhanced by lowering the measurement temperature and reached ~−3.0%.

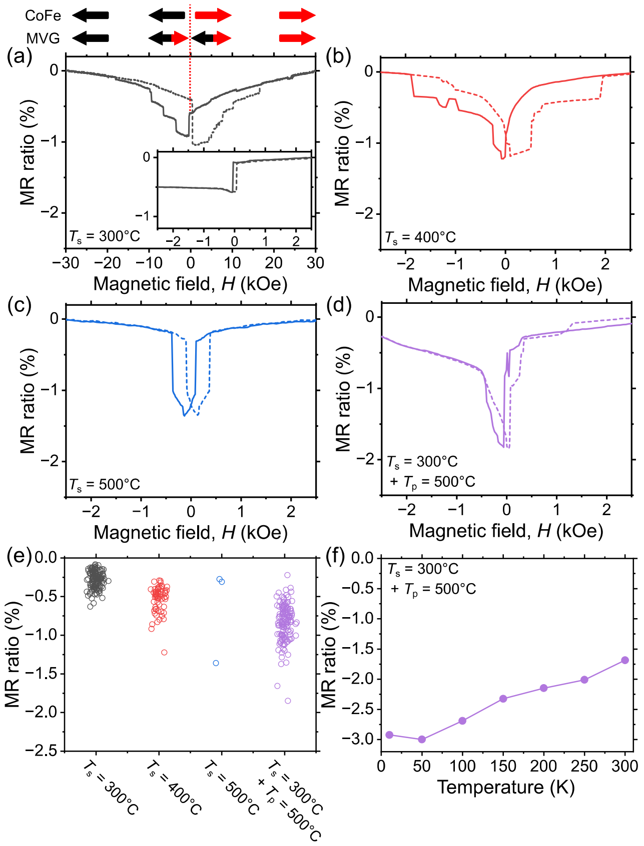

Fig. 4. (a)–(d) Examples of the *R*-*H* curves measured in the CPP-GMR devices fabricated from the series-C samples for $T_s = 300$ºC, 400ºC, 500ºC and $T_s = 300$ºC + $T_p = 500$ºC. The solid and dashed lines represent the downward and upward *H* sweeps, respectively. The schematics above (a) depict the magnetization configurations of the MVG and CoFe layers for the upward *H* sweep, and the inset in (a) shows the minor loop measured in the smaller *H* range. (e) Annealing condition dependence of MR ratio of all the devices. (f) Measurement temperature dependence of MR ratio for $T_s = 300$ºC + $T_p = 500$ºC.

To confirm that the negative MR was obtained in the GMR stack properly fabricated as designed, we observed the cross-sectional microstructure of the series-C sample for $T_s = 300°C + T_p = 500°C$. Figures 5(a) and 5(b) show a HAADF-STEM image and EDS mapping, respectively. The results confirm sharp and flat interfaces between the layers without noticeable interdiffusion. The thicknesses of the layers were close to the designed values. Figure 5(c) shows the EDS line profile along the growth direction. The MVG layer composition was estimated to be $Mn_{54.8}V_{20.5}Ga_{24.8}$, which was in good agreement with the XRF results. The CoFe layer composition was close to $Co_{50}Fe_{50}$, as designed. Figure 5(d) shows the NBED patterns obtained in the MVG layer. The 002 and 111 superlattice spots were observed, confirming the existence of the $B2$ and $L2_1$ ordering. Figure 5(e) shows the atomic-resolution HAADF-STEM image and the corresponding Fourier-transform filtered image obtained at the upper interface of MVG with Ag. An atomically flat matched interface was observed. The interface has a few dislocations marked by $\perp$ symbols. Figure 5(f) shows the similar results at the lower interface of MVG with W. The lower interface was rougher than the upper interface, indicating that the flatness was improved in the MVG layer by appropriate thermal treatment.

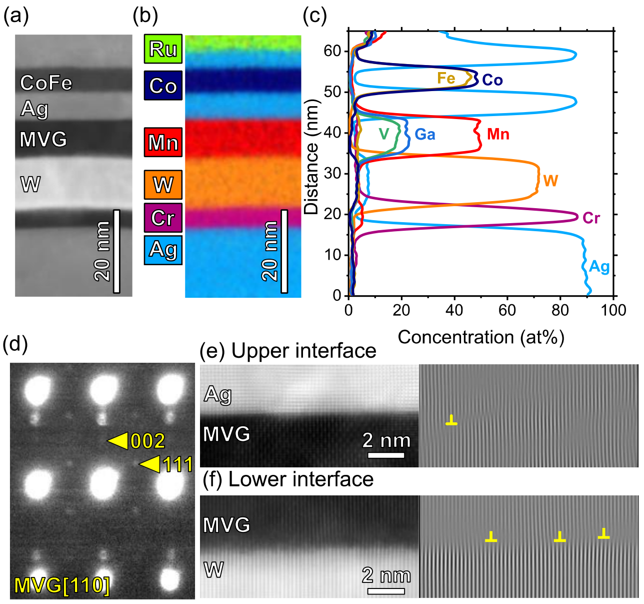

Fig. 5. (a) HAADF-STEM image and (b) EDS mapping of the series-C sample for $T_s = 300$ºC + $T_p = 500$ºC. (c) EDS line profile obtained from (b). (d) NBED patterns obtained in the MVG layer. (e) Atomic-resolution HAADF-STEM image and the corresponding Fourier-transform filtered image obtained at (e) the upper interface of MVG with Ag and (f) the lower interface of MVG with W. The yellow ⊥ symbols indicate dislocations.

Finally, we calculated the transmittance of MVG/Ag/MVG(001) to examine the Fermi surface matching of MVG with Ag spacer for utilizing the negative spin polarization of MVG. Figures 6(a) and 6(b) show in-plane wave vector dependence of the minority-spin transmittance in the parallel magnetization configuration for Mn and VGa termination, respectively. We confirmed that the magnetic structure of MVG in MVG/Ag/MVG(001) is consistent with that of bulk $L2_1$-MVG obtained in the previous work[35]. The transmittance originates dominantly from the minority-spin channel, reflecting the negative spin polarization of MVG. From the transmittance, the interfacial RA was calculated to be 6.97 mΩ·μm^2 for Mn termination and 5.86 mΩ·μm^2 for VGa termination. For comparison, we refer to the cases of Co$_2$FeGa$_{0.5}$Ge$_{0.5}$ / Ag / Co$_2$FeGa$_{0.5}$Ge$_{0.5}$(001), in which a high MR ratio has been reported experimentally. The interfacial

RA of majority-spin electron in this systems was calculated to be 1.77, 1.69, and 2.32 mΩ·μm^2 for FeGa, FeGe and, Co termination, respectively [12,44] , which are much lower than that of minority-spin electron in MVG / Ag / MVG(001). It has been reported that the calculated interfacial RA and experimental MR ratio have negative correlation; the lower RA tends to have higher MR ratio [45]. Therefore, relatively high interfacial RA of MVG / Ag / MVG(001) reflecting weak hybridization between Ag and Mn (V) orbitals suggests that the Ag spacer is not suitable for MVG, which partly explains the small magnitude of negative MR ratio obtained in this study. Further research is necessary to find an optimal spacer material.

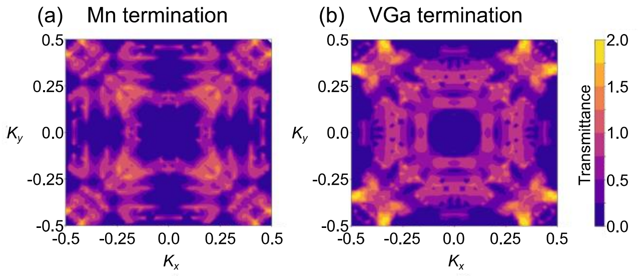

Fig. 6. In-plane wave vector dependence of the minority-spin transmittance in parallel magnetization configuration calculated for Mn_2VGa / Ag / $Mn_2VGa(001)$ with (a) Mn termination and (b) VGa termination.

This work demonstrated the negative MR ratio in the epitaxial MVG/Ag/CoFe pseudo-spin-valve CPP-GMR devices, providing evidence of the negative spin polarization in MVG. Despite the large device-to-device distributions in the measured MR ratio within each sample, reflecting the variations in the field response and ordering of the MVG layer in the small device area, the MR ratio exhibited a statistical change with the annealing conditions and was enhanced in the following order: T_s = 300ºC, T_s = 400ºC, and T_s = 300ºC + T_p = 500ºC. This trend coincides with the trend of M_s for these thermal treatments, and the increase in the MR ratio is attributed to both reduced H_s and improved ordering by optimizing the annealing conditions. The maximum MR value at room temperature was ~−1.8 % for T_s = 300ºC + T_p = 500ºC. Note that this value is underestimated because of the incomplete antiparallel configuration. Interestingly, the *R*-*H* curves for T_s = 300ºC showed a large hysteresis, and the MVG layer acted as a fixed magnetic layer in the minor loop measured in the small *H* range. This behavior is applicable to sensor operation, though the MR ratio is small. According to the T_s dependence of M_s shown in Fig. 2(b), T_s = 500ºC and above significantly improved the ordering of the MVG grown on the MgO substrates or W layers. However, such an annealing condition increased the roughness and was unsuitable for the CPP-GMR stacks. In addition, the transmittance calculation indicated that the Ag spacer is not suitable for MVG. In these aspects, the potential of MVG has not been fully exploited. To this end, suitable template materials to facilitate ordering and improve the flatness of MVG, adjusting MVG composition to promote ordering at lower temperatures, optimal thermal treatments, and suitable spacer materials needs to be further studied.

IV CONCLUSIONS

We studied the negative spin polarization of MVG in epitaxial pseudo-spin-valve CPP-GMR devices. We used a W insertion layer to prevent interdiffusion between the MVG layer and the low-resistance Ag bottom electrode. The MVG layer on the W layer exhibited similar M_s to those on MgO substrates, indicating that the W layer did not disturb the ordering of MVG. We fabricated the GMR stack consisting of MVG/Ag/CoFe, and TEM observation confirmed the sharp and flat interfaces between each layer without noticeable interdiffusion. Negative MR ratio was observed in the CPP-GMR devices, and the MR value changed with thermal treatments because the thermal treatments affected the ordering, roughness, and magnetic properties of MVG. The maximum negative MR ratio was approximately –1.8% at room temperature. This value is the highest negative MR reported in pseudo-spin-valve CPP-GMR devices, even though it is underestimated due to the incomplete antiparallel magnetization configuration. These results demonstrated the potential of MVG as a material with high negative spin polarization.

SUPPLEMENTARY MATERIAL

The supplementary material explains TEM and XRD data of CPP-GMR stack using Cr/Ag bottom electrodes and distributions of R and MR in all the devices fabricated on series-C sample for T_s = 300ºC + T_p = 500ºC.

ACKNOWLEDGMENTS

This work was partially supported by Advanced Storage Research Consortium (ASRC), JSPS KAKENHI Grant No. 21K20434, and No. 23K03934, and MEXT Initiative to Establish Next-generation Novel Integrated Circuits Centers (X-nics) Grant No. JPJ011438. The authors thank Dr. T. Kubota of Tohoku University for fruitful discussions and M. Inoue of NIMS for technical support. The calculations in this study were performed on the Numerical Materials Simulator at NIMS.

CONFLICT OF INTEREST STATEMENT

The authors declare no conflicts of interest associated with this manuscript.

DATA AVAILABILITY SATATEMENT

The data that support the findings of this study are available from the corresponding author upon reasonable request.

References

[1] J. C. Slonczewski, *Current-Driven Excitation of Magnetic Multilayers*, J. Magn. Magn. Mater. **159**, L1 (1996).

[2] L. Berger, *Emission of Spin Waves by a Magnetic Multilayer Traversed by a Current*, Phys. Rev. B **54**, 9353 (1996).

[3] S. I. Kiselev, J. C. Sankey, I. N. Krivorotov, N. C. Emley, R. J. Schoelkopf, R. A. Buhrman, and D. C. Ralph, *Microwave Oscillations of a Nanomagnet Driven by a Spin-Polarized Current*, Nature **425**, 380 (2003).

[4] M. Hosomi et al., *A Novel Nonvolatile Memory with Spin Torque Transfer Magnetization Switching: Spin-RAM*, Tech. Dig. - Int. Electron Devices Meet. IEDM **2005**, 459 (2005).

[5] F. Macià, A. D. Kent, and F. C. Hoppensteadt, *Spin-Wave Interference Patterns Created by Spin-Torque Nano-Oscillators for Memory And*, Nanotechnology **22**, 095301 (2011).

[6] J. Torrejon et al., *Neuromorphic Computing with Nanoscale Spintronic Oscillators*, Nat. 2017 5477664 **547**, 428 (2017).

[7] T. Kanao, H. Suto, K. Mizushima, H. Goto, T. Tanamoto, and T. Nagasawa, *Reservoir Computing on Spin-Torque Oscillator Array*, Phys. Rev. Appl. **12**, (2019).

[8] Y. Sakuraba, M. Hattori, M. Oogane, Y. Ando, H. Kato, A. Sakuma, T. Miyazaki, and H. Kubota, *Giant Tunneling Magnetoresistance in Co2MnSi/Al-O /Co 2MnSi Magnetic Tunnel Junctions*, Appl. Phys. Lett. **88**, 10 (2006).

[9] H. Liu, Y. Honda, T. Taira, K. Matsuda, M. Arita, T. Uemura, and M. Yamamoto, *Giant Tunneling Magnetoresistance in Epitaxial Co2MnSi/MgO/Co2MnSi Magnetic Tunnel Junctions by Half-Metallicity of Co2MnSi and Coherent Tunneling*, Appl. Phys. Lett. **101**, 132418 (2012).

[10] S. Li, Y. K. Takahashi, T. Furubayashi, and K. Hono, *Enhancement of Giant Magnetoresistance by L21 Ordering in Co2Fe(Ge0.5Ga0.5) Heusler Alloy Current-Perpendicular-to-Plane Pseudo Spin Valves*, Appl. Phys. Lett. **103**, 042405 (2013).

[11] M. Jourdan et al., *Direct Observation of Half-Metallicity in the Heusler Compound Co2MnSi*, Nat. Commun. **5**, 3974 (2014).

[12] J. W. Jung, Y. Sakuraba, T. T. Sasaki, Y. Miura, and K. Hono, *Enhancement of Magnetoresistance by Inserting Thin NiAl Layers at the Interfaces in Co2FeGa0.5Ge0.5/Ag/Co2FeGa0.5Ge0.5 Current-Perpendicular-to-Plane Pseudo Spin Valves*, Appl. Phys. Lett. **108**, 102408 (2016).

[13] S. Andrieu, A. Neggache, T. Hauet, T. Devolder, A. Hallal, M. Chshiev, A. M. Bataille, P. Le Fèvre, and F. Bertran, *Direct Evidence for Minority Spin Gap in the <math> <mrow> <mi Mathvariant="normal">C</Mi> <msub> <mi Mathvariant="normal">o</Mi> <mn>2</Mn> </Msub> <mi>MnSi</Mi> </Mrow> </Math> Heusler Compound*, Phys. Rev. B **93**, 094417 (2016).

[14] K. Elphick, W. Frost, M. Samiepour, T. Kubota, K. Takanashi, H. Sukegawa, S. Mitani, and A. Hirohata, *Heusler Alloys for Spintronic Devices: Review on Recent Development and Future Perspectives*, Sci. Technol. Adv. Mater. **22**, 235 (2021).

[15] K. Hamaya and M. Yamada, *Semiconductor Spintronics with Co2-Heusler Compounds*, MRS Bull. **47**, 584 (2022).

[16] M. AlHajDarwish, H. Kurt, S. Urazhdin, A. Fert, R. Loloee, W. P. Pratt, and J. Bass, *Controlled Normal and Inverse Current-Induced Magnetization Switching and Magnetoresistance in Magnetic Nanopillars*, Phys. Rev. Lett. **93**, 157203 (2004).

[17] H. Suto, T. Nakatani, N. Asam, H. Iwasaki, and Y. Sakuraba, *Evaluation of Spin-Transfer-Torque Efficiency Using Magnetization Reversal against a Magnetic Field: Comparison of FeCr with Negative Spin Polarization and NiFe*, Appl. Phys. Express **16**, 013003 (2023).

[18] J.-G. Zhu, X. Zhu, and Y. Tang, *Microwave Assisted Magnetic Recording*, IEEE Trans. Magn. **44**, 125 (2008).

[19] S. Bosu, H. Sepehri-Amin, Y. Sakuraba, S. Kasai, M. Hayashi, and K. Hono, *High Frequency Out-of-Plane Oscillation with Large Cone Angle in Mag-Flip Spin Torque Oscillators for Microwave Assisted Magnetic Recording*, Appl. Phys. Lett. **110**, 142403 (2017).

[20] W. Zhou, H. Sepehri-Amin, T. Taniguchi, S. Tamaru, Y. Sakuraba, S. Kasai, H. Kubota, and K. Hono, *Inducing Out-of-Plane Precession of Magnetization for Microwave-Assisted Magnetic Recording with an Oscillating Polarizer in a Spin-Torque Oscillator*, Appl. Phys. Lett. **114**, 172403 (2019).

[21] N. Asam, H. Suto, S. Tamaru, H. Sepehri-Amin, A. Bolyachkin, T. Nakatani, W. Zhou, H. Kubota, and Y. Sakuraba, *Analysis Method of a Spin-Torque Oscillator Using Dc Resistance Change during Injection Locking to an External Microwave Magnetic Field*, Appl. Phys. Lett. **119**, 142405 (2021).

[22] M. Takagishi, N. Narita, H. Iwasaki, H. Suto, T. Maeda, and A. Takeo, *Design Concept of MAS Effect Dominant MAMR Head and Numerical Study*, IEEE Trans. Magn. **57**, 3300106 (2021).

[23] Y. Nakagawa, M. Takagishi, N. Narita, A. Takeo, and T. Maeda, *Multiple Spin Injection Into Coupled Field Generation Layers for Low Current Operation of MAMR Heads*, IEEE Trans. Magn. **58**, 3201005 (2022).

[24] K. Sunaga, M. Tsunoda, K. Komagaki, Y. Uehara, and M. Takahashi, *Inverse Tunnel Magnetoresistance in Magnetic Tunnel Junctions with an Fe4N Electrode*, J. Appl. Phys. **102**, 013917 (2007).

[25] S. Yasui, S. Honda, J. Okabayashi, T. Yanase, T. Shimada, and T. Nagahama, *Large Inverse Tunnel Magnetoresistance in Magnetic Tunnel Junctions with an <math Display="inline" Overflow="scroll"> <msub> <mi>Fe</Mi> <mn>3</Mn>*

</Msub> <msub> <mrow> <mrow> <mi Mathvariant="normal">O</Mi> </Mrow> </Mrow> <mn>4</Mn> </Msub> </Math> Ele, Phys. Rev. Appl. **15**, 034042 (2021).

[26] C. Bellouard, H. Rapp, B. George, S. Mangin, G. Marchal, and J. Ousset, *Negative Spin-Valve Effect i/A Trilayers*, Phys. Rev. B - Condens. Matter Mater. Phys. **53**, 5082 (1996).

[27] C. Vouille, A. Barthélémy, F. E. Mpondo, A. Fert, P. A. Schroeder, S. Y. Hsu, A. Reilly, and R. Loloee, *Microscopic Mechanisms of Giant Magnetoresistance*, Phys. Rev. B - Condens. Matter Mater. Phys. **60**, 6710 (1999).

[28] X. Li, H. Li, M. Jamali, and J.-P. Wang, *Damping Constant Measurement and Inverse Giant Magnetoresistance in Spintronic Devices with Fe4N*, AIP Adv. **7**, 125303 (2017).

[29] H. Suto, T. Nakatani, Y. Kota, A. Nagarjuna, H. Iwasaki, K. Amemiya, T. Mitsui, S. Sakai, S. Li, and Y. Sakuraba, *Study on FeCr Thin Film for a Spintronic Material with Negative Spin Polarization*, J. Magn. Magn. Mater. **557**, 169474 (2022).

[30] K. Ramesh Kumar, N. Harish Kumar, G. Markandeyulu, J. A. Chelvane, V. Neu, and P. D. Babu, *Structural, Magnetic and Transport Properties of Half-Metallic Ferrimagnet Mn2VGa*, J. Magn. Magn. Mater. **320**, 2737 (2008).

[31] K. Ramesh Kumar, N. Harish Kumar, P. D. Babu, S. Venkatesh, and S. Ramakrishnan, *Investigation of Atomic Anti-Site Disorder and Ferrimagnetic Order in the Half-Metallic Heusler Alloy Mn 2 V Ga*, J. Phys. Condens. Matter **24**, 336007 (2012).

[32] C. Klewe, M. Meinert, J. Schmalhorst, and G. Reiss, *Negative Spin Polarization of Mn2VGa Probed by Tunnel Magnetoresistance*, J. Phys. Condens. Matter **25**, 76001 (2013).

[33] K. Ozdogan, I. Galanakis, E. Şaşioglu, and B. Aktaş, *Search for Half-Metallic Ferrimagnetism in V-Based Heusler Alloys Mn 2VZ (Z ≤ Al, Ga, In, Si, Ge, Sn)*, J. Phys. Condens. Matter **18**, 2905 (2006).

[34] L. Wollmann, S. Chadov, J. Kübler, and C. Felser, *Magnetism in Cubic Manganese-Rich Heusler Compounds*, Phys. Rev. B **90**, 214420 (2014).

[35] L. Fan, F. Chen, C. Li, X. Hou, X. Zhu, J. Luo, and Z.-Q. Chen, *Promising Spintronics: Mn-Based Heusler Alloys Mn3Ga, Mn2YGa (Y = V, Nb, Ta), ScMnVGa*, J. Magn. Magn. Mater. **497**, 166060 (2020).

[36] Z. H. Li et al., *Enhancing Atomic Ordering, Magnetic and Transport Properties of Mn2VGa Heusler Alloy Thin Films toward Negatively Spin-Polarized Charge Injection*, Acta Mater. **276**, 120110 (2024).

[37] N. Narita, M. Takagishi, H. Iwasaki, H. Suto, G. Koizumi, A. Takeo, and T. Maeda, *Design and Numerical Study of Flux Control Effect Dominant MAMR Head: FC Writer*, IEEE Trans. Magn. **57**, 3300205 (2021).

[38] R. Landauer, *Electrical Resistance of Disordered One-Dimensional Lattices*, Philos. Mag. **21**, 863 (1970).

[39] P. Giannozzi et al., *QUANTUM ESPRESSO: A Modular and Open-Source Software Project for Quantum Simulations of Materials*, J. Phys. Condens. Matter **21**, 395502 (2009).

[40] P. Giannozzi et al., *Advanced Capabilities for Materials Modelling with Quantum ESPRESSO*, J. Phys. Condens. Matter **29**, 465901 (2017).

[41] J. P. Perdew, K. Burke, and M. Ernzerhof, *Generalized Gradient Approximation Made Simple*, Phys. Rev. Lett. **77**, 3865 (1996).

[42] J. W. Jung, Z. Jin, Y. Shiokawa, and M. Sahashi, *Investigations of Interface Spin Asymmetry and Interfacial Resistance in Fe x Co100 − x /Ag Interface*, J. Appl. Phys. **117**, 17A323 (2015).

[43] T. Seki, H. Iwama, T. Shima, and K. Takanashi, *Size Dependence of the Magnetization Reversal Process in Microfabricated L1 0 -FePt Nano Dots*, J. Phys. D. Appl. Phys. **44**, 335001 (2011).

[44] K. Simalaotao, Y. Miura, and Y. Sakuraba, *Origin of the Difference in Spin-Dependent Transport Properties between Half-Metallic Co2FeGa0.5Ge0.5 and Co2Mn0.5Fe0.5Si with the Ag Spacer*, Prep. (n.d.).

[45] Y. Miura, *First-Principles Studies on Spin-Dependent Transport of Magnetic Junctions with Half-Metallic Heusler Compounds*, J. Magn. Soc. Japan **47**, 2307R005 (2023).

Supplementary material

Negative spin polarization of Mn_2VGa Heusler alloy thin films studied in current-perpendicular-to-plane giant magnetoresistance devices

Hirofumi Suto, Vineet Barwal, Kodchakorn Simalaotao, Zehao Li, Keisuke Masuda, Taisuke Sasaki, Yoshio Miura, and Yuya Sakuraba

Research Center for Magnetic and Spintronic Materials, National Institute for Materials Science (NIMS), Tsukuba, 305-0047, Japan

STEM observation and XRD of CPP-GMR stack containing a Cr/Ag bottom electrode

Figures S1(a) show the structure of the CPP-GMR stack containing a Cr/Ag bottom electrode and a 20-nm-thick MVG layer deposited at 550ºC. Figures S1(b) and S1(c) show a HAADF-STEM image and EDS mapping, respectively. The TEM observation shows the formation of Ag columns penetrating the MVG layer, disrupting the designed layer structure. Because The layers above the MVG layer were deposited at room temperature after cooling down, their structure was not damaged. The electrical current is expected to flow preferentially through the Ag columns, and this stack is not suitable to evaluate the spin polarization of MVG. Figure S1(d) shows the EDS line profile obtained from the region where MVG layer exist. A small amount of Mn and Ga was detected in the whole Ag bottom electrode. This diffusion of Mn and Ga into the Ag bottom electrode is consistent with the phase diagram of Ag-Mn and Ag-Ga system, which shows small amount of Mn and Ga is miscible to Ag at the annealing temperature. Figure S1(e) shows the EDS line profile obtained from the region with the Ag column. The composition of the column though the MVG layer is almost the same as that of the bottom electrode.

Figures S2(a) and S2(b) show the out-of-plane and [111]-direction XRD profiles. Despite the disrupted layer structure, (001)-oriented growth of the MVG layer was maintained, and 002 and 111 super lattice peaks were observed.

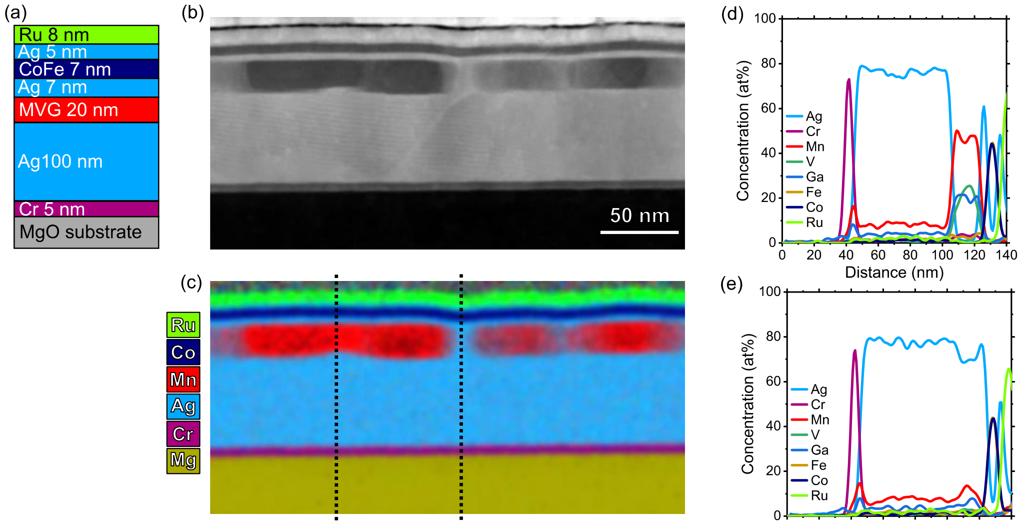

FIG. S1. (a) Structure of the CPP-GMR stack containing a Cr/Ag bottom electrode and a MVG layer. (b) HAADF-STEM image and (c) EDS mapping. EDS line profile obtained from (d) the region where MVG layer exist and (e) the region with Ag column through the MVG layer. The dotted lines in (c) shows the position of the EDS line profiles.

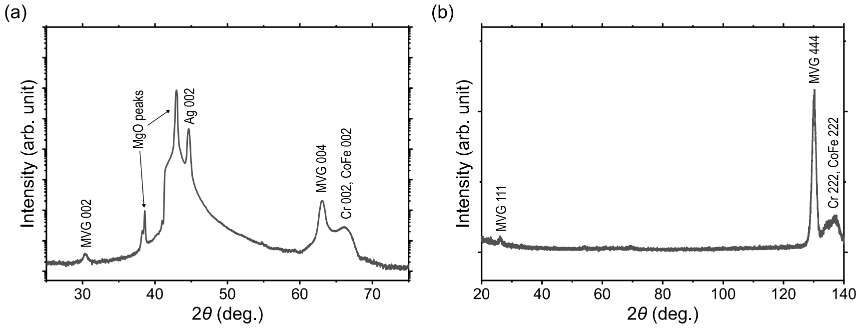

FIG. S2. (a) Out-of-plane and (b) [111]-direction XRD profiles of the CPP-GMR stack shown in Fig. S1.

Resistance and MR ratio distribution of CPP-GMR devices for T_s = 300ºC + T_p = 500ºC

Figures S3 show the R_{max} and MR ratio of the 75 devices with dimensions of (a) 80 nm × 80 nm and (b) 140 nm × 70 nm fabricated from the series-C samples for T_s = 300ºC + T_p = 500ºC, respectively. The data from 5 devices showing abnormal R were excluded from the analysis.

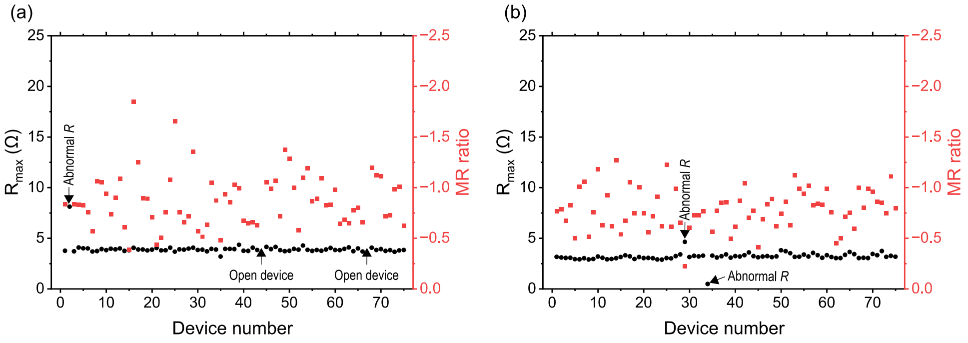

FIG. S3. R_{max} and MR ratio of the devices fabricated the series-C samples for T_s = 300ºC + T_p = 500ºC. The device size is 80 nm × 80 nm in (a) and 140 nm × 70 nm in (b).